Bioinspiration & Biomimetics

PAPER • OPEN ACCESS

Bio-inspired all-optical artificial neuromast for 2D flow sensing

View the article online for updates and enhancements.

Bioinspiration & Biomimetics

PAPER

Bio-inspired all-optical artificial neuromast for 2D flow sensing

Ben J Wolf[1], Jonathan A S Morton[2], William N MacPherson[2] and Sietse M van Netten[1]

[1] Institute of Artificial Intelligence and Cognitive Engineering, University of Groningen, Groningen, Netherlands
[2] School of Engineering and Physical Sciences, Heriot-Watt University, Riccarton, Edinburgh, United Kingdom

E-mail: b.j.wolf@rug.nl

Abstract

We present the design, fabrication and testing of a novel all-optical 2D flow velocity sensor, inspired by a fish lateral line neuromast. This artificial neuromast consists of optical fibres inscribed with Bragg gratings supporting a fluid force recipient sphere. Its dynamic response is modelled based on the Stokes solution for unsteady flow around a sphere and found to agree with experimental results. Tuneable mechanical resonance is predicted, allowing a deconvolution scheme to accurately retrieve fluid flow speed and direction from sensor readings. The optical artificial neuromast achieves a low frequency threshold flow sensing of $5 \, \text{mm s}^{-1}$ and $5 \, \mu\text{m s}^{-1}$ at resonance, with a typical linear dynamic range of 38 dB at 100 Hz sampling. Furthermore, the optical artificial neuromast is shown to determine flow direction within a few degrees.

1. Introduction

The design of our optical sensor is directly inspired by a sensory modality used for flow detection by aquatic vertebrates. Fish and amphibians have an array of discrete mechanical sensors at their disposal called neuromasts, which are distributed along the head and trunk. With these neuromasts they can perceive a 1D projection of local fluid motion or flow relative to the body (Dijkgraaf 1963). The biophysical properties of neuromasts, such as the interplay of physiology, mechanics and fluid dynamics, have been studied intensively elsewhere (van Netten 2006, van Netten and McHenry 2013).

There are two types of neuromasts, each with their beneficial physical properties to help the fish perceive freestream (DC) and dynamic or oscillatory (AC) flow (Bleckmann *et al* 2004). Superficial neuromasts (SN) are present on the surface of the body and are in direct contact with the surrounding medium. They are tailored to perceive steady (DC) and low frequency fluid flow velocity. The canal neuromasts (CN) are not in direct contact with the freestream flow, but are housed in internal canals. They are deflected through the pressure difference via flexible membranes or pores in these canals, thereby effectively perceiving freestream (AC) fluid acceleration.

The perceived local fluid flow at each neuromast over time can be concatenated to a spatiotemporal flow pattern, which augments the fish sensory perception (Curcic-Blake and van Netten 2006). This enables fish to sense fluid perturbations generated by moving sources. In fish behavioural experiments, the lateral line has been shown to be instrumental in many specific behaviours, for instance, prey detection, schooling behaviour, and spatial orientation (Coombs and Montgomery 1999, Ghysen and Dambly-Chaudiere 2007, Tao and Yu 2012).

In order to mimic this biological near-field sensing, several implementations of artificial neuromast sensors have been developed, which also measure a 1D projection of local fluid flow. Some sensors make use of hot wire anemometry (Pandya *et al* 2006, Yang *et al* 2006). Here, a suspended hot nanowire is cooled down by fluid flow. This links a measureable change in the temperature dependent resistance to fluid flow speed. Most artificial SNs, however, rely on sensing generated strain at the base of a deflecting lamella or cantilever structure in response to fluid flow. This design is favoured since the protruding structures escape unwanted boundary layer effects. Several techniques used for strain sensing include lamella mechanical micro-sensors (MEMs) (Fan *et al* 2002, McConney *et al* 2009, Yang *et al* 2007, 2010), ionic polymer-metal composites (IPMC) (Abdulsadda and Tan 2012, 2013, Chen *et al* 2013) and soft polymer membranes without (Asadnia *et al* 2013) and with cantilever structures (Kottapalli *et al* 2014, Asadnia *et al* 2015, Kottapalli *et al* 2015). A technical review of recent contributions to the field of artificial neuromast and artificial lateral lines (ALL) shows an increasing interest in this field (Liu *et al* 2016). In some cases, orientations of 1D-sensitive
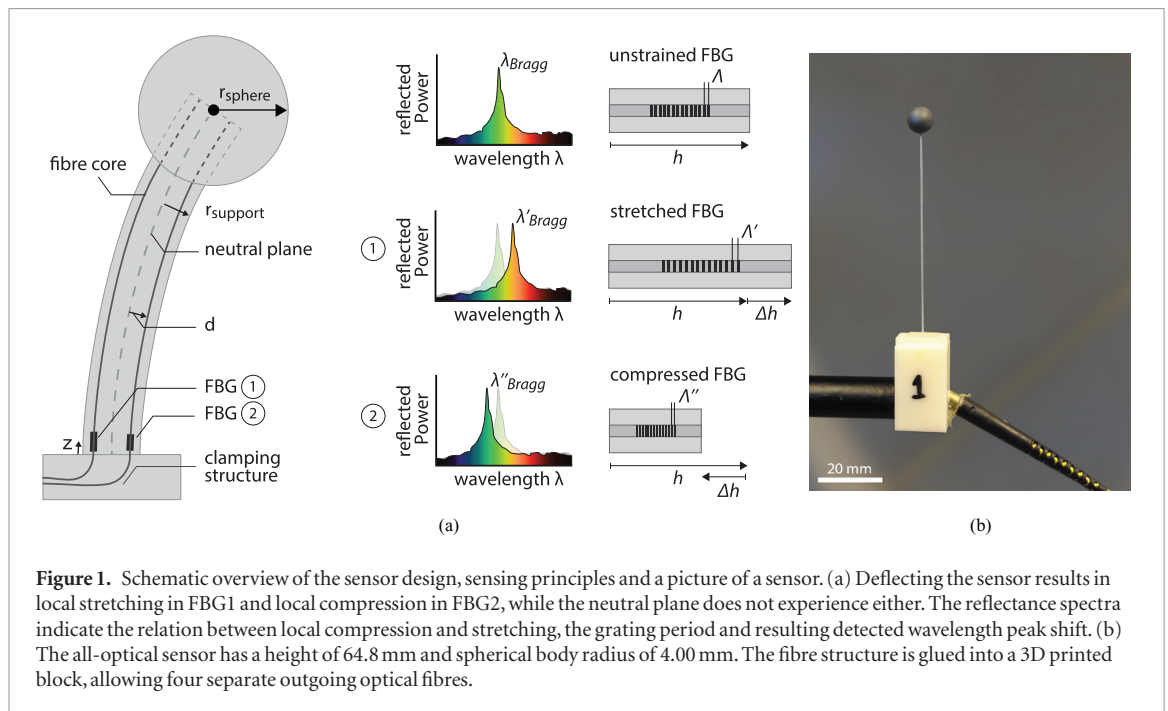
Figure 1. Schematic overview of the sensor design, sensing principles and a picture of a sensor. (a) Deflecting the sensor results in local stretching in FBG1 and local compression in FBG2, while the neutral plane does not experience either. The reflectance spectra indicate the relation between local compression and stretching, the grating period and resulting detected wavelength peak shift. (b) The all-optical sensor has a height of 64.8 mm and spherical body radius of 4.00 mm. The fibre structure is glued into a 3D printed block, allowing four separate outgoing optical fibres.

sensors are alternated to sense multiple projections, allowing measuring flow perpendicular to the array, e.g. Yang *et al* (2010) and Ahrari *et al* (2017).

These SN designs rely on electric methods to operate in wet conditions. Because electric signals are susceptible to noise pickup over large distances, deployment of remote and large scale artificial lateral lines (ALL) has been somewhat limited. We therefore present an all-optical artificial neuromast which aims to address these issues. Our design utilises fibre Bragg gratings (FBGs), which allows the sensor data to be transmitted through fibre optic cables, thereby enhancing the scalability for all-optical ALLs. Furthermore, our design enables two dimensional fluid flow measurements, thus increasing the information per point measurement.

FBGs are sections in an optical fibre that have been modified to include a periodic variation in the refractive index along the fibre length. This structure reflects light at a specific wavelength that is determined by the spacing of the FBG structure. Stretching or compressing the fibre changes the FBG structure spacing and therefore increases or decreases the reflected wavelength. If the FBG is illuminated with a broadband optical source containing a wide range of wavelengths then the reflected (Bragg) wavelength can be interpreted as a function of the applied strain.

Different geometries consisting of two or more optical fibres glued together have been used in order to determine the curvature of the end position of the combined fibre structure (Araujo *et al* 2002). This requires the gratings to be located outside the neutral (bending) axis of a cantilever structure. Examples of FBG curvature sensors (Flockhart *et al* 2003) and accelerometers (Fender *et al* 2007) have also been developed using multicore optical fibres with multiple cores positioned away from the neutral axis.

Cantilever Bragg grating flow sensing has been used for monitoring steady flow rates (Lu and Chen 2008) and flow perturbations in response to a bluff body (Takashima *et al* 2004) in pipes. However, the dynamic properties of the sensors were not examined.

We first present a combined hydrodynamics and strain-structure model which enables sensor characteristics such as its mechanical sensitivity and frequency response to be predicted. Using steady state contact deflection, we infer the linear dynamic range of the sensor. Finally, through hydrodynamically stimulating the sensor at different frequencies, we verify the sensor characteristics and employ a related method to reconstruct flow speeds from sensor readings.

2. Sensor and fluid model

2.1. Sensor design
The sensor physically resembles a fluid force recipient spherical body and a fibre support structure providing elastic coupling (figure 1(a)). To model the signal of a deflecting sensor, the elastic support is treated as an end-loaded cantilever beam. Using Bernoulli's beam equations, we model the support with length h, having a circular cross section, and possessing flexural stiffness EI (with Young's modulus E and the second moment of area I).

2.2. FBG sensing
Equations (2.1) and (2.2) show the relationship between the force F applied at a beams tip, the resulting tip displacement magnitude $\Delta \tau$ and the generated strain ϵ at a distance d from the neutral bending axis at a height z from the fixed cantilever end (Benham *et al* 1996). The beam is compressed in the bending direction, which decreases strain. On the opposite side of the bending axis, where the sign of d is opposite, the beam stretches locally, increasing strain.
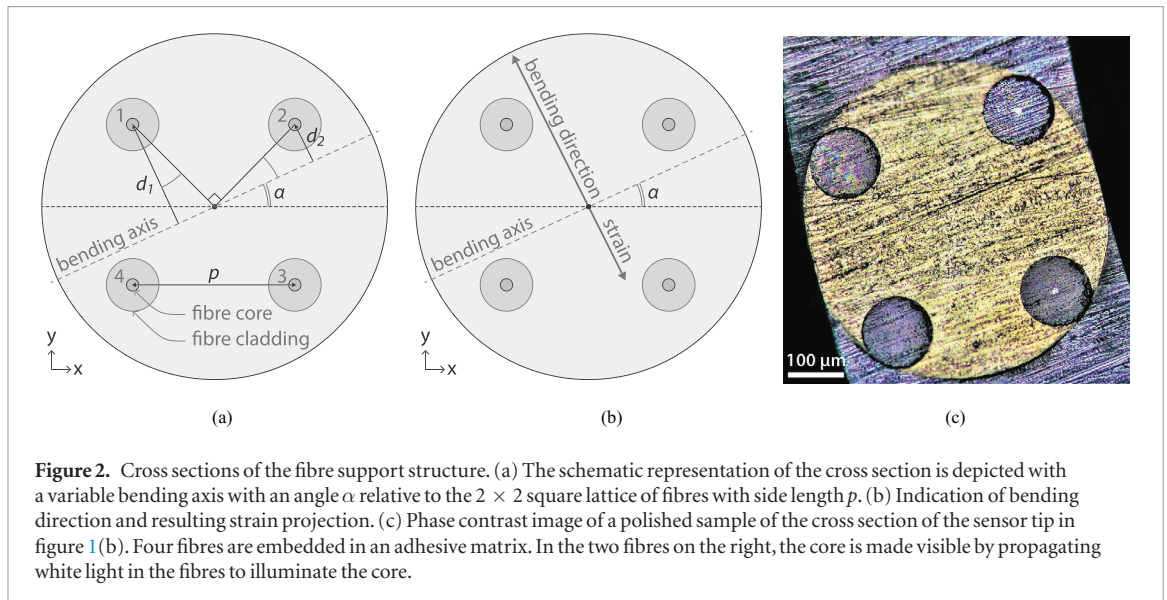
Figure 2. Cross sections of the fibre support structure. (a) The schematic representation of the cross section is depicted with a variable bending axis with an angle α relative to the 2×2 square lattice of fibres with side length p. (b) Indication of bending direction and resulting strain projection. (c) Phase contrast image of a polished sample of the cross section of the sensor tip in figure 1(b). Four fibres are embedded in an adhesive matrix. In the two fibres on the right, the core is made visible by propagating white light in the fibres to illuminate the core.

$$\Delta \tau = \frac{F}{EI} \frac{h^3}{3} \qquad (2.1)$$

$$\epsilon = -\Delta \tau \cdot \frac{3 \cdot d \cdot (h - z)}{h^3}. \qquad (2.2)$$

This strain is measured locally via FBGs (figure 1(a)). The FBG comprises a periodic refractive index modulation with a period on the scale of the wavelength of light, such that it reflects light at the Bragg wavelength, λ_B, which is twice the inter-grating distance or grating period Λ.

$$\epsilon = \frac{\Delta h}{h} = \frac{\Delta \Lambda}{\Lambda} = \frac{\Delta \lambda_B}{\lambda_B}. \qquad (2.3)$$

The Bragg wavelength changes as a function of strain (equation (2.3)) and temperature (Hill and Meltz 1997). The thermal effect can be compensated using differential strain configurations in which the thermal effect is common to all considered gratings (Flockhart *et al* 2003). Both the local Bragg wavelength shifts (i.e. sensor signal) and sensor deflections can be practically obtained to ascertain to what extent these are consistent with our present model. Common FBG wavelengths are in the communications band and we choose to work with gratings in this region of $\lambda_B = 1560 \pm 40$ nm.

2.3. Isotropic sensor mechanics

The support comprises four discrete standard communication SMF-28 fibres, where the light guiding core is centred in a silica outer cladding. The mechanical properties of the fibre support structure are largely determined by the bending stiffness K which is, apart from sensor height, governed by the geometry and composition of the cross section of the elastic support.

Since the support matrix and fibres form a composite material, its flexural stiffness EI depends on the mechanical properties of both materials. The added flexural stiffness of each fibre depends on its

squared distance to the neutral bending axis (Benham *et al* 1996). Although the bending axis may rotate by deflecting the sensor in different directions, we show below that the flexural stiffness—and therefore the bending stiffness K—is independent of a variable bending axis offset α.

In order to show that the flexural stiffness is circular symmetric, only fibres 1 and 2 are considered, since the cross section is mechanically symmetrical above and below the bending axis. When the sensor is deflected over an axis with a variable offset angle α compared to the square lattice, the individual distances d_1, d_2 between the fibres and the bending axis change. But since they form sides of an identical right angle triangle, their summed squared distance to the bending axis ($d_1^2 + d_2^2 = p^2/2$) remains constant and is independent of α. It is only dependent on a fixed p, the distance between two adjacent fibre cores. The flexural stiffness of the support is therefore mechanically circularly symmetric; no preferred bending direction exists.

This results in a direction independent, or isotropic, bending stiffness K determined at the tip of the fibre structure

$$K = \frac{3\pi}{4 \cdot h^3} \left[E_s \cdot r_s^4 + 4 \left(E_c - E_s \right) \left(r_c^2 \cdot p^2 + r_c^4 \right) \right], \qquad (2.4)$$

where r_c and r_s denote the cladding and support radii and E_c and E_s their respective Young's moduli.

Similarly, in this square lattice configuration (figure 2(b)), we show below that the magnitude of a differential strain vector $\overrightarrow{\delta \epsilon}$, generated by a fixed magnitude of tip deflection $\Delta \tau$, is not affected by a variable bending axis offset α. First, we can define the fibre distances $d_1 = \cos(\pi/4 - \alpha) \sqrt{2} \cdot p/2$, $d_2 = \sin(\pi/4 - \alpha) \sqrt{2} \cdot p/2, d_3 = -d_1$ and $d_4 = -d_2$. When deflecting the sensor, with an offset bending axis α, in the direction $\alpha + \pi/2$ and using equation (2.2), the Cartesian differential strain projections then become

$$\delta\epsilon_x = \epsilon_2 - \epsilon_1$$

$$= C\left[\sin\left(\frac{\pi}{4} - \alpha\right) - \cos\left(\frac{\pi}{4} - \alpha\right)\right] \quad (2.5)$$

$$= C \cdot -\sqrt{2} \cdot \cos\left(\alpha - \frac{\pi}{2}\right),$$

$$\delta\epsilon_y = \epsilon_2 - \epsilon_3$$

$$= C\left[\sin\left(\frac{\pi}{4} - \alpha\right) + \cos\left(\frac{\pi}{4} - \alpha\right)\right] \quad (2.6)$$

$$= C \cdot -\sqrt{2} \cdot \sin\left(\alpha - \frac{\pi}{2}\right),$$

with

$$C = \frac{-\Delta\tau \cdot 3 \cdot (h - z) \cdot \sqrt{2} \cdot p}{2 \cdot h^3}, \quad (2.7)$$

where ϵ_n denotes the generated strain at core number n. Then, working out the magnitude and angle of differential strain in polar coordinates, we find that

$$r_{\delta\epsilon} = \Delta\tau \cdot \frac{3 \cdot p \cdot (h - z)}{h^3}, \text{ and} \quad (2.8)$$

$$\theta_{\delta\epsilon} = \alpha - \frac{\pi}{2}. \quad (2.9)$$

The absolute differential strain magnitude $r_{\delta\epsilon}$ shows that we can generalise the use of individual fibre distances d to the inter-fibre distance p in case of differential strain c.f. equation (2.2) & (2.8). Furthermore, the direction $\theta_{\delta\epsilon}$ of increased differential strain lags the bending axis by $\pi/2$ and is therefore opposite to the bending direction, which is consistent with equation (2.2).

Since the strain vector $\overrightarrow{\delta\epsilon}$ is opposite to to the bending vector (figure 2(b)), and we aim to measure flow speeds in the bending direction, we choose a pairing of sensor cores such that the projection of differential wavelength shift $(\overrightarrow{\delta\lambda} \propto -\overrightarrow{\delta\epsilon})$ is in the bending direction. With respect to the sensor orientation as depicted in figure 2, the Cartesian projections of wavelength difference are given by

$$\delta\lambda_x = c_1 - c_2 = c_4 - c_3 = G \cdot \Delta\tau_x, \quad (2.10)$$

$$\delta\lambda_y = c_3 - c_2 = c_4 - c_1 = G \cdot \Delta\tau_y, \quad (2.11)$$

where c_n denotes the generated Bragg wavelength shift at core number n. Alternative combinations of cores, such as along the diagonals of the lattice, also provide the required orthogonality. This diagonal combination requires four functional cores and is therefore less redundant.

The induced differential wavelength shift $\overrightarrow{\delta\lambda}$ and deflection $\overrightarrow{\Delta\tau}$ can conveniently be defined as vectors and are thus only a dimensionless linear geometrical factor apart (equation (2.12)).

$$G = \frac{|\overrightarrow{\delta\lambda}|}{|\overrightarrow{\Delta\tau}|} = \frac{3 \cdot p \cdot (h - z) \cdot \lambda_B}{h^3}. \quad (2.12)$$

Using practical values for p of tenths of millimetres, combined with sensor height h in the order of centimetres, the value of G is typically in the order of 10^{-7}.

2.4. Dynamic properties

The physical parameters of both the elastic support and sensor body can be adjusted to predict and obtain desirable dynamic and filter characteristics. We obtain the frequency dependent sensitivity of the sensor by adapting a model for CNs found in fish (van Netten 2006). The magnitude of the complex frequency response $\text{FR}(f)$ is defined as the frequency dependent ratio of sensor response (in this case sensor body motion) per unit fluid velocity. Its argument constitutes the frequency dependent phase lag. In this model, given the relative dimensions of the sensor body and fibre support, we neglect fluid forces acting on the support.

Only three independent physical parameters determine the frequency response: the transition frequency f_t, which selectively shifts a constant shaped Bode plot along the frequency axis, a resonance number N_r, which determines the shape of the associated Bode plot, and the novel buoyancy factor b of the sensor body, which also affects the Bode plot shape. The frequency response and its parameters are described by equations (2.13)–(2.16).

$$\text{FR}(f) = \frac{1}{2\pi f_t} \cdot$$

$$\frac{1 + \frac{\sqrt{2}}{2}(1 + i)\left(\frac{f}{f_t}\right)^{\frac{1}{2}} + \frac{1}{3}i\frac{f}{f_t}}{N_r + i\frac{f}{f_t} - \frac{\sqrt{2}}{2}(1 - i)\left(\frac{f}{f_t}\right)^{\frac{3}{2}} - \frac{2}{9}(b + \frac{1}{2})\left(\frac{f}{f_t}\right)^2} \quad (2.13)$$

$$f_t = \frac{\mu}{2 \cdot \pi \cdot \rho_{\text{fluid}} \cdot a^2} \quad (2.14)$$

$$N_r = \frac{K \cdot a \cdot \rho_{\text{fluid}}}{6 \cdot \pi \cdot \mu^2} \quad (2.15)$$

$$b = \frac{\rho_{\text{body}}}{\rho_{\text{fluid}}}. \quad (2.16)$$

The sensor is a dampened resonator; its resonant character is parameterized by N_r and affected by the bending stiffness K, sensor body radius a, fluid viscosity μ, fluid density ρ_{fluid}, and body density ρ_{body}.

The resonance frequency f_r (equation (2.17)) indicates the frequency at which the maximum of the FR is located. The resonating behaviour is quantified through the quality (Q) factor (equation (2.18)), which only depends on N_r. Keeping the Q factor low causes the sensor low pass filter function (i.e. frequency response) to remain as flat as possible, effectively increasing its useable bandwidth.

$$f_r \cong f_t \cdot \sqrt{N_r \cdot \frac{9}{2} \cdot \frac{1}{b + \frac{1}{2}}} \quad (2.17)$$

$$Q = \frac{f_r}{\Delta f} \cong \sqrt{\frac{2}{3}} \cdot \left(\frac{N_r}{3}\right)^{\frac{1}{4}}. \quad (2.18)$$

The bandwidth itself is bounded by a cut-off frequency f_c, the frequency at which the response in the fall-off region matches the DC response and is given by

$$f_c = f_t \cdot N_r \cdot \sqrt{\frac{3}{2(b + \frac{1}{2})}}. \qquad (2.19)$$

2.5. Design optimisation

Using the dynamic and mechanical properties, we can optimise some sensor parameters with respect to fluid sensing. With $FR(f = 0)$, the response at low frequencies can be found. Together with the cut-off frequency this leads to a sensitivity-bandwidth (SB) product, which only depends on b:

$$SB = FR(0) \cdot f_c = \frac{1}{2\pi} \cdot \sqrt{\frac{3}{2(b + \frac{1}{2})}}. \quad (2.20)$$

The SB is clearly maximal when $b = 0$, then $SB = \sqrt{3}/(2\pi)$, which is an 73% increase compared to neutrally buoyant neuromasts as found in fish (van Netten and McHenry 2013). Using polyethylene spheres with an effective b of about 0.05 in water at room temperature, allows for an increase of SB of about 65% over neutrally buoyant sensors.

Given the geometric factor (equation (2.12)) and the frequency response (equation (2.17)) at low frequencies, we can also optimise the generated differential wavelength shift per fluid velocity by varying the inter-fibre distance p.

$$\frac{|\overrightarrow{\delta\lambda}|}{V} = \frac{24 \cdot a \cdot \mu \cdot p \cdot (h - z) \cdot \lambda_B}{\left[E_s r_s^4 + 4\left(E_c - E_s\right)\left(r_c^2 p^2 + r_c^4\right)\right]} \cdot (2.21)$$

In equation (2.21), it is reflected in the numerator that the wavelength shift per fluid velocity increases linearly with the core distance p. However, the optical fibres have to be compressed and stretched at effectively larger distances, adding to the flexural and therefore bending stiffness which is reflected in the denominator with a factor of p^2. As a consequence, p has an optimal value for maximising detected wavelength shift per fluid velocity at

$$p_{opt} = \frac{1}{r_c} \cdot \sqrt{\frac{E_s \cdot r_s^4}{4(E_c - E_s)} + r_c^4}. \qquad (2.22)$$

With the chosen materials and related Young's moduli, this optimal distance is smaller than the core diameter. Therefore the optimal design has the fibres as close as possible to each other. Fabrication constraints limited the practical separation of the fibres to a minimum of $p = 0.3$ mm.

3. Methods

In the manufacturing process, four standard communication optical SMF-28 fibres (jackets removed, $r_c = 62.5$ μm, $E_c = 75$ GPa) are suspended in a square column formation. This leaves room for the optical adhesive to flow around the fibres. A custom glue dispenser and UV-curing system is encapsu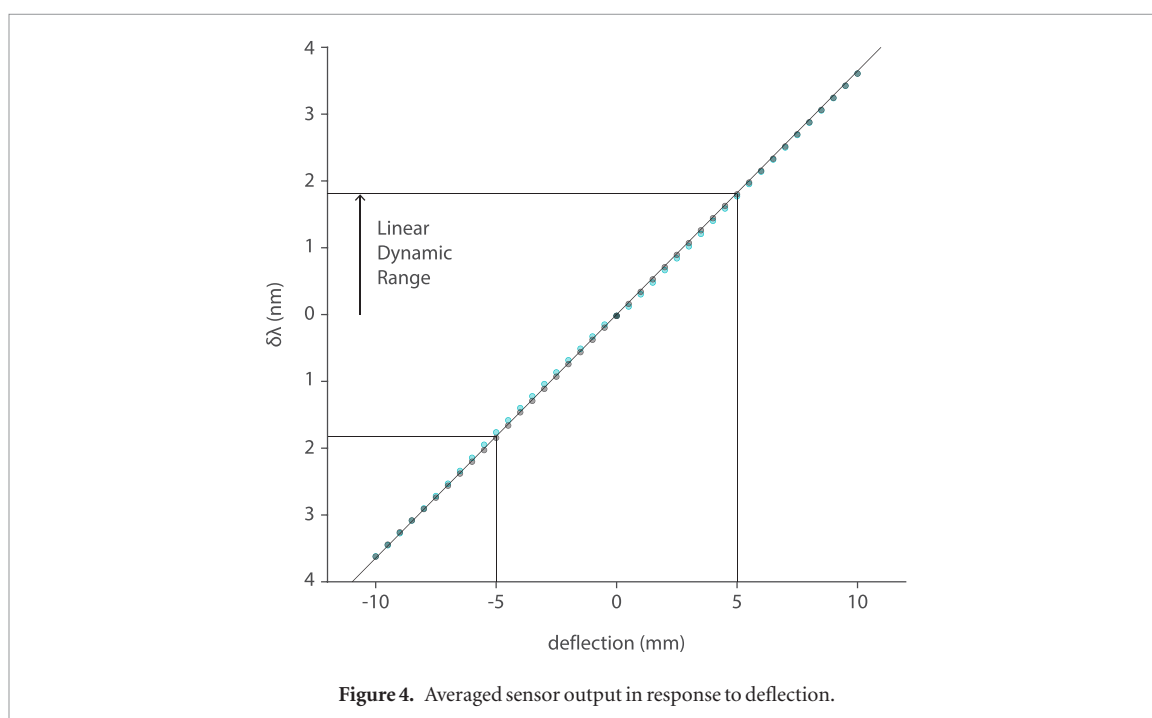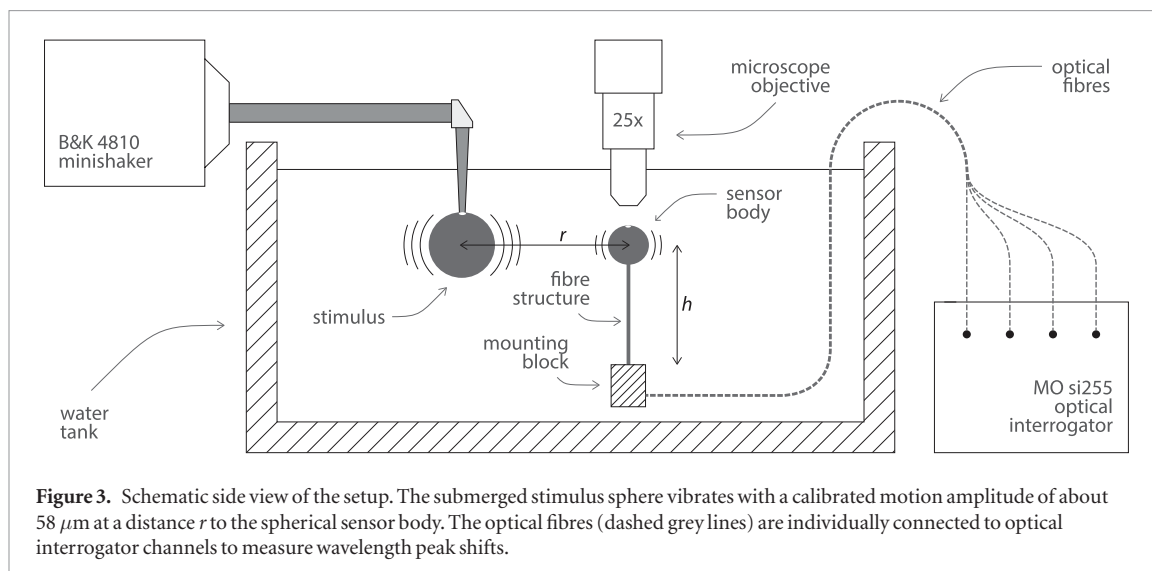lating the four fibres and is slowly moved along the fibre formation. This embeds the fibres in a matrix ($E_s = 0.14$ GPa) of UV-cured optical adhesive (NOA68, Norland Products Cranbury, NJ, USA). A cross section of the resulting fibre structure is shown in figure 2(c). The fibre structure is then glued into a mounting block using an epoxy adhesive, in which a small diameter hole acts as a fixed cantilever point for the sensor. The sensor with length $h = 64.8$ mm is fitted with a polyethylene sphere $a = 4.00$ mm, $b = 0.05$.

Figure 2(c) shows a cross section of the tip of the support structure, which is the closest indication of the cross section at the FBG height z. Here, the average distance between the fibre cores is found to be $p = 313.1 \pm 5.4$ μm. The optical fibres do not form a perfect square, therefore we can expect some variation of bending stiffness depending on the bending direction. With the average radius of the support $r_s = 277.4 \pm 5.5$ μm, and the centre of the inscribed FBG sections located at $z = 5$ mm, we expect a geometrical factor (equation (2.12)) of $G = 3.22 \pm 0.05 \cdot 10^{-7}$, which describes the relation between the generated differential wavelength shift (sensor signal) per deflection at height h. On the basis of the dynamic properties described in section 2.4, we expect the sensor to have a resonance frequency of 13.4 Hz and a Q factor of 13.4.

First, we validated that the sensor response is linear in our operational range by mechanically deflecting the sensor. This allows for a linear relation between sensor body motion and resulting optical signals via a geometric factor, and is a requirement for acquiring the frequency response FR using the current method. Using a linear stage, the sensor was deflected in steps of 0.5 mm while monitoring the sensor signal. Then, in order to infer its dynamic properties, i.e. the FR, the sensor motion and sensor signal were monitored in response to a hydrodynamic dipole stimulus (figure 3).

Sensor body motion was measured with a calibrated Zeiss Axiotron microscope. A 2D position sensitive detector (On-Trak PSM 2-2) allowed for high-speed 2D tracking of an attached reflectance marker within a range of 500 μm $\times$ 500 μm in the objective focal plane. Strain-induced FBG wavelength peak shift was measured with picometer resolution at 5 kHz using an optical interrogator (Micron Optics si225, Atlanta, USA). The difference in reflectance peaks of cores 1 and 2 and those of core 4 and 1 (figure 2(a)) are used as Cartesian x and y projections of measured wavelength shifts (equations (2.10) and (2.11)).

A hydrodynamic dipole source was produced using a Bruel & Kjaer 4810 mini-shaker driving a submerged sphere ($\oslash = 9.9$ mm). This stimulus was levelled with the sensor height h. The water tank setup (figure 3) was placed on a vibration isolation table (Newport VW series) as to avoid mechanical noise. Sinusoidal stimuli were generated, and sensor body motion synchronously acquired, using a CED power1401 data acquisition system. The mini-shaker was calibrated for

Figure 3. Schematic side view of the setup. The submerged stimulus sphere vibrates with a calibrated motion amplitude of about 58 μm at a distance *r* to the spherical sensor body. The optical fibres (dashed grey lines) are individually connected to optical interrogator channels to measure wavelength peak shifts.

Figure 4. Averaged sensor output in response to deflection.

frequencies ranging from 1 to 200 Hz, with a constant travel amplitude of about 58 μm. A model for viscous flow (van Netten 2006) was used for calculating the fluid flow velocity produced by the calibrated stimulus. The stimulus sphere was positioned at a distance *r*, measured using a micrometer stage.

The sensor was pre-stimulated diagonally at a given stimulation frequency for at least 3 seconds before sampling, in order to avoid transients. For both sensor motion and sensor signal, we obtained the amplitude and phase lag by applying a flat-top window suitable for low amplitude and resolution data (Heinzel *et al* 2002), and calculating the discrete Fourier transform. From the resulting spectrum magnitude, we take the maximal value at the stimulation frequency as the response amplitude. The corresponding imaginary part yields the phase-lag at that frequency. In order to prevent spectral aliasing in Fourier analysis, 64 low pass filtered

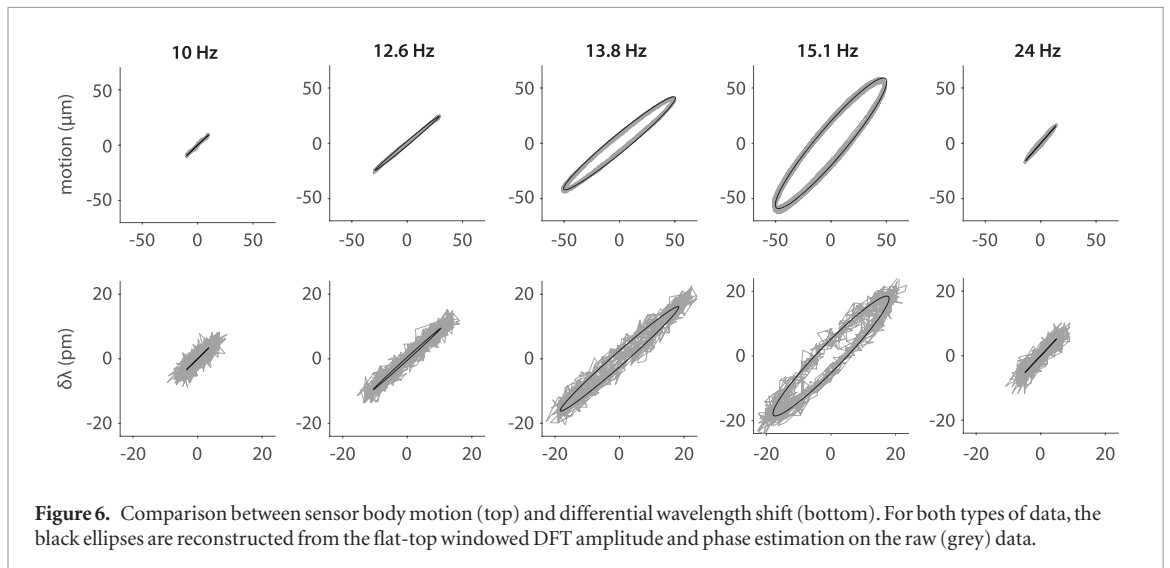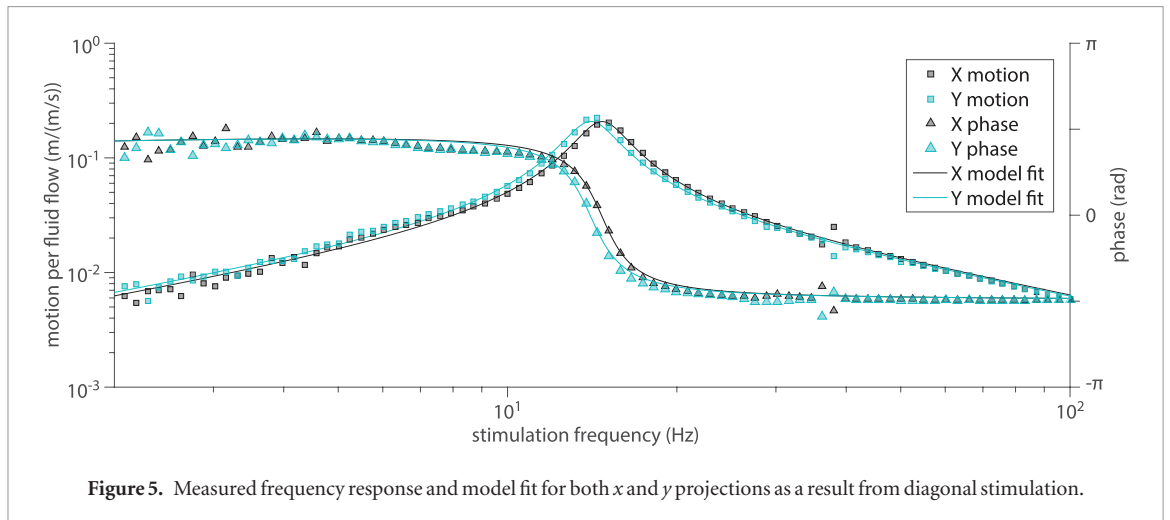periods of sensor motion with 512 samples per period were sampled for a given stimulation frequency.

4. Results

The Cartesian (*x*, *y*) sensor signals for a sensor at rest showed normal distributed noise on the measured differential wavelengths with a standard deviation of 2.02 pm at 5 kHz sampling, which defines a lower bound for the dynamic range of the sensor.

4.1. Linearity

To test for linearity, the sensor has been deflected in steps of 0.5 mm up to 10 mm (black) and back to origin (cyan) for both positive and negative deflections, where each position was held for at least four seconds.

From figure 4, we infer that the sensor response is linear for deflections up to 5 mm as a conservative

Figure 5. Measured frequency response and model fit for both *x* and *y* projections as a result from diagonal stimulation.

Figure 6. Comparison between sensor body motion (top) and differential wavelength shift (bottom). For both types of data, the black ellipses are reconstructed from the flat-top windowed DFT amplitude and phase estimation on the raw (grey) data.

estimate ($R^2 > 0.999$), and approximately linear up to 10 mm with some small deviations. On average, a deflection of 5 mm corresponds to a differential wavelength shift of 1.78 nm. The slope of the response matching this linear part yields a measured geometric factor (equation (2.12)) of $3.56 \cdot 10^{-7}$ under static deflection conditions.

4.2. Dynamic response

To determine the frequency response and further verify the geometric factor at dynamic submillimetre deflections, the sensor was hydrodynamically stimulated at frequencies from 2 to 100 Hz. Figure 5 shows the frequency response for the sensor body motion in the *x* and *y* directions.

Here, the *x* (black) and *y* (cyan) projections of measured sensor body motion (squares) and phase (triangles) are plotted for each stimulation frequency. Their respective fits result in the fitted parameters $b = 0.05$, $f_t = 0.021$, $N_{r,x} = 7.12 \cdot 10^4$ and $N_{r,y} = 6.52 \cdot 10^4$.

The measured frequency response (figure 5) shows a slight difference in resonance peaks and phase lag for the *x* and *y* directions. From this measurement, we find that the sensor has a resonance frequency of 14.7 Hz in

its *x* direction, with a *Q* factor of 15.3. In the *y* direction, we find a resonance frequency of 14.0 Hz and a slightly lower *Q* factor of 15.1. This slight difference is most visible near the phase flip and amplitude maxima and is reflected in their different fitted values for N_r. This difference can therefore be attributed to the mechanical properties of the non-perfect square lattice inside the fibre support structure; a slight directional difference exists.

Figure 6 shows the wavelength shift signal and body motion over time of five trials of the frequency response measurement. As expected, the relative orientation and magnitude of both types of data match up. From the ratio of sensor signal amplitude to sensor motion amplitude, we obtain a measured geometric factor of $3.58 \cdot 10^{-7}$ in the submillimetre domain under dynamic conditions.

Due to the small directional difference in bending stiffness and resulting frequency response, the *x* and *y* projections of motion, and therefore sensor signal, have a slight phase lag difference. This produces sensor motion in ellipses rather than straight lines at stimulation close to either *x* or *y* resonance frequencies. In the next section we demonstrate a method to correct for this phenomenon.
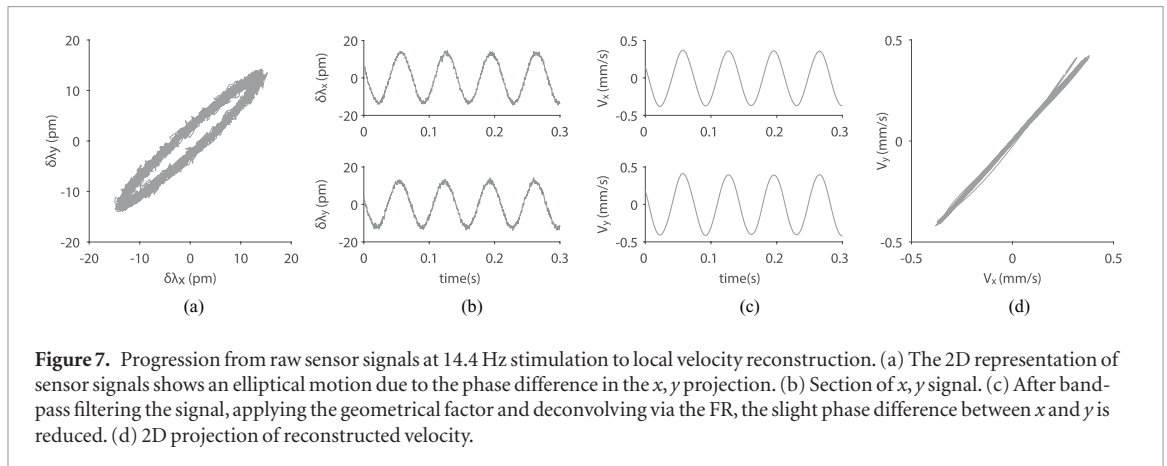
Figure 7. Progression from raw sensor signals at 14.4 Hz stimulation to local velocity reconstruction. (a) The 2D representation of sensor signals shows an elliptical motion due to the phase difference in the x, y projection. (b) Section of x, y signal. (c) After band-pass filtering the signal, applying the geometrical factor and deconvolving via the FR, the slight phase difference between x and y is reduced. (d) 2D projection of reconstructed velocity.

5. Discussion

The measured sensor behaviour has been shown to compare well with the modelled input-output and frequency characteristics. The sensor acts as a dampened resonator both driven and dampened by fluid forces. The results show that the measured frequency response (figure 5) is accurately described by the combined hydrodynamics and strain-structure model. Both large, static, mechanical deflection ($G = 3.56 \cdot 10^{-7}$) and small, dynamic, hydrodynamical stimulation ($G = 3.58 \cdot 10^{-7}$) aligns with the modelled mechanical properties of the sensor based on the cross section from the sensor tip ($G = 3.22 \pm 0.05 \cdot 10^{-7}$).

This model can therefore be used to relate sensor signal via sensor body motion to local fluid flow in two steps. First, the sensor signal can be translated to sensor body motion with the geometric factor G. Then, by a deconvolution via the frequency response (equation (2.13)), which incorporates the fluid-dynamic characteristics of the sensor, we can accurately obtain the local 2D flow velocity (see figure 7).

5.1. Sensitivity and dynamic range

The measurement of the frequency characteristics in figure 5 shows an expected peak, which indicates the resonance frequency, where the sensor is most sensitive. Higher frequencies will be filtered out, i.e. there's a constant downward slope in the frequency response curve. At frequencies below resonance, the frequency response plateaus and will still pick up low frequency and DC flow (see equation (2.19) and table 1), although it is not specifically designed to do so.

The lowest detectable flow speeds of the artificial neuromasts affect the detection limits for tracking objects using artificial lateral lines (Boulogne *et al* 2017). We can infer this threshold velocity, at which the expected sensor signal equals noise levels, by taking the ratio of the measured noise in $\overrightarrow{\delta\lambda}$ to G times the frequency response (table 1).

When down sampling the signal by averaging with a factor 50, the noise levels dropped from 2.02 pm to 0.28 pm with a factor close to $\sqrt{50}$, as would be

Table 1. Lowest detectable fluid velocities for the optical sensor. The lower frequency sensitivities are extrapolated from the fitted model and indicated with a *. Both x, y resonance frequencies are displayed to indicate the magnitude of difference between sensing low frequency flow and flow at sensor resonance.

Sampling	5 kHz		100 Hz	
V (mm s^{-1})	V_x	V_y	V_x	V_y
0 Hz*	36	34	5.1	4.8
0.01 Hz*	22	21	3.2	3.0
0.1 Hz*	9.1	8.5	1.3	1.2
1 Hz*	1.7	1.6	0.23	0.22
10 Hz	0.11	0.098	0.016	0.014
14.0 Hz^y	0.031	0.027	0.0043	0.0039
14.7 Hz^x	0.028	0.030	0.0039	0.0043
50 Hz	0.42	0.44	0.059	0.062

expected from normally distributed noise. The sensor is shown to be linear up to deflections of about 5 mm (figure 4). Taking the corresponding 1.78 nm wavelength shift and σ_{noise} as the upper and lower boundaries respectively, this amounts to a linear Dynamic Range of 29 dB at 5 kHz sampling and 38 dB when down sampled to 100 Hz.

5.2. Two-dimensional fluid flow sensing

Two orthogonal projections of flow can be measured by the all-optical artificial neuromast using the information of at least three cores. This requires that four fibres are positioned in a square lattice embedded in a support structure. The sensor cross section as shown in figure 2(c) shows that the centres of the four fibres do not form a perfect square, so some directional variance in stiffness and therefore sensitivity exists. By employing a 2D method of sensing sensor body motion, we can measure, and correct for, this directional variance. In practice, by processing the sensor signals via a deconvolution along two orthogonal dimensions, we can translate sensor signal and body motion with their respective phase lag and resonance properties to a 2D representation of local fluid flow.

Figure 7 shows the deconvolution process (for details, see Smith (1997)). Here, measured sensor signals are first band pass filtered in order to reduce high

and low frequency noise. In the frequency domain, the real sensor amplitudes are divided by the amplitudes of the FR. The FR phase is subtracted from the imaginary valued sensor phase information. Using an inverse Fourier transform, the resulting amplitude and phase information is then transformed back into the time domain. For longer or continuous sensor readings, taking a small buffer period into account, this procedure can be performed real-time using sliding time windows.

In addition, we can express the uncertainty of the sensor readings both in Cartesian projections of measured fluid flow as well as a magnitude and direction representation. As is clear from figure 7(d), the reconstructed velocity contains some magnitude and direction variance. Ignoring velocity readings under 0.05 mm s^{-1} and taking the ratio of V_x and V_y over time, the variation in the reconstructed direction of velocity oscillation amounts to a standard deviation of $\sigma = 1.8°$, with an oscillating flow amplitude of 0.54 mm s^{-1}. The sensor is therefore able to reliably determine fluid flow direction within a few degrees.

6. Conclusion

We have shown that the fibre structure mechanically acts in accordance with our combined hydrodynamics and strain-structure model. The predictable nature of dynamic behaviour allows for deconvolution of measured strain induced FBG signals via the frequency dependent velocity sensitivity which, in turn, allows for direct translation to fluid velocity. The dynamic characteristics are tuneable by varying the sensor dimensions and mechanical properties, allowing a tailored design for specific use cases.

The presented strain-structure model allows optimizing the sensor design for generating strain and thus sensor signal per sensor motion. The observed geometric factor relating sensor body motion to observed differential wavelength shift is in accordance with the modelled geometric factor. It is consistent throughout the measurements and allows individual sensors to be calibrated by using conventional displacement sensitive methods, such as mechanical deflection or visual monitoring.

A welcome enhancement from its 1D-sensitive biological counterpart and state-of-the-art artificial neuromasts is that by interrogating the sensor in two perpendicular axes, a single sensor will provide information about both the magnitude and the angle of the local flow velocity. Although it is shown that stationary artificial lateral lines can reconstruct dipole sources and moving artificial lateral lines can detect obstacles without a second dimension, this extra information might be able to increase the ALL detection precision and effectiveness.

Acknowledgments

ORCID iDs

Ben J Wolf ⬛ https://orcid.org/0000-0002-8024-5352

References

Abdulsadda A T and Tan X 2012 An artificial lateral line system using IPMC sensor arrays *Int. J. Smart Nano Mater.* **3** 226–42

Abdulsadda A T and Tan X 2013 Nonlinear estimation-based dipole source localization for artificial lateral line systems *Bioinspiration Biomimetics* **8** 026005

Ahrari A, Lei H, Sharif M A, Deb K and Tan X 2017 Reliable underwater dipole source characterization in 3d space by an optimally designed artificial lateral line system *Bioinspiration Biomimetics* **12** 036010

Araujo F M, Ferreira L A and Santos J L 2002 Simultaneous determination of curvature, plane of curvature, and temperature by use of a miniaturized sensing head based on fiber Bragg gratings *Appl. Opt.* **41** 2401–7

Asadnia M, Kottapalli A G P, Miao J, Warkiani M E and Triantafyllou M S 2015 Artificial fish skin of self-powered micro-electromechanical systems hair cells for sensing hydrodynamic flow phenomena *J. R. Soc. Interface* **12** 20150322

Asadnia M, Kottapalli A G P, Shen Z, Miao J and Triantafyllou M 2013 Flexible and surface-mountable piezoelectric sensor arrays for underwater sensing in marine vehicles *IEEE Sensors J.* **13** 3918–25

Benham P P, Armstrong C and Crawford R J 1996 *Mech. Eng. Mater.* (Reading, MA: Addison-Wesley)

Bleckmann H, Mogdans J, Engelmann J, Kröther S and Hanke W 2004 Wie fische wasser fühlen: das seitenliniensystem *Biologie Unserer Zeit* **34** 358–65

Boulogne L H, Wolf B J, Wiering M A and van Netten S M 2017 Performance of neural networks for localizing moving objects with an artificial lateral line *Bioinspir. Biomim.* **12** 056009

Chen X, Zhu G, Yang X, Hung D L S and Tan X 2013 Model-based estimation of flow characteristics using an ionic polymer metal composite beam *IEEE/ASME Trans. Mechatron.* **18** 932–43

Coombs S and Montgomery J C 1999 The enigmatic lateral line system *Comparative Hearing: Fish, Amphibians* vol 11, ed R R Fay *et al* (New York: Springer) pp 319–62

Curcic-Blake B and van Netten S M 2006 Source location encoding in the fish lateral line canal *J. Exp. Biol.* **209** 1548–59

Dijkgraaf S 1963 The functioning and significance of the lateral-line organs *Biol. Rev.* **38** 51–105

Fan Z, Chen J, Zou J, Bullen D, Liu C and Delcomyn F 2002 Design and fabrication of artificial lateral line flow sensors *J. Micromech. Microeng.* **12** 655

Fender A *et al* 2007 Two-axis accelerometer based on multicore fibre Bragg gratings *Proc. 3rd European Workshop on Optical Fibre Sensors* p 6619

Flockhart G M H, MacPherson W N, Barton J S, Jones J D C, Zhang L and Bennion I 2003 Two-axis bend measurement with Bragg gratings in multicore optical fiber *Opt. Lett.* **28** 387

Ghysen A and Dambly-Chaudiere C 2007 The lateral line microcosmos *Gen. Dev.* **21** 2118–30

Heinzel G, Rüdiger A and Schilling R 2002 Spectrum and spectral density estimation by the Discrete Fourier transform (DFT), including a comprehensive list of window functions and some new at-top windows (submitted version available at: https://holometer.fnal.gov/GH_FFT.pdf)

Hill K O and Meltz G 1997 Fiber Bragg grating technology fundamentals and overview *J. Lightwave Technol.* **15** 1263–76

Kottapalli A G P, Asadnia M, Hans H, Miao J M and Triantafyllou M S 2014 Harbor seal inspired MEMS artificial micro-whisker sensor *IEEE 27th Int. Conf. on Micro Electro Mechanical Systems* (IEEE) pp 741–4

Kottapalli A G P, Asadnia M, Miao J and Triantafyllou M 2015 Soft polymer membrane micro-sensor arrays inspired by the

mechanosensory lateral line on the blind cavefish *J. Intell. Mater. Syst. Struct.* **26** 38–46

Liu G, Wang A, Wang X and Liu P 2016 A review of artificial lateral line in sensor fabrication and bionic applications for robot fish *Appl. Bionics Biomech.* **2016** 1–15

Lu P and Chen Q 2008 Fiber Bragg grating sensor for simultaneous measurement of flow rate and direction *Meas. Sci. Technol.* **19** 125302

McConney M E, Chen N, Lu D, Hu H A, Coombs S, Liu C and Tsukruk V V 2009 Biologically inspired design of hydrogel-capped hair sensors for enhanced underwater flow detection *Soft Matter* **5** 292–5

Pandya S, Yang Y, Jones D L, Engel J and Liu C 2006 Multisensor processing algorithms for underwater dipole localization and tracking using MEMS artificial lateral-line sensors *EURASIP J. Adv. Signal Process.* **2006** 1–9

Smith S W 1997 Chapter 17: custom filters *The Scientist and Engineer's Guide to Digital Signal Processing* (San Diego, CA: California Technical Publishing) pp 297–310

Takashima S, Asanuma H and Niitsuma H 2004 A water flowmeter using dual fiber Bragg grating sensors and cross-correlation technique *Sensors Actuators* A **116** 66–74

Tao J and Yu X B 2012 Hair flow sensors: from bio-inspiration to bio-mimickinga review *Smart Mater. Struct.* **21** 113001

van Netten S M 2006 Hydrodynamic detection by cupulae in a lateral line canal: functional relations between physics and physiology *Biol. Cybern.* **94** 67–85

van Netten S M and McHenry M J 2013 The biophysics of the fish lateral line *The Lateral Line System* vol 48, ed S Coombs *et al* (New York: Springer) pp 99–119

Yang Y, Chen J, Engel J, Pandya S, Chen N, Tucker C, Coombs S, Jones D L and Liu C 2006 Distant touch hydrodynamic imaging with an artificial lateral line *Proc. Natl Acad. Sci.* **103** 18891–5

Yang Y, Chen N, Tucker C, Engel J, Pandya S and Liu C 2007 From artificial hair cell sensor to artificial lateral line system: development and application *IEEE 20th Int. Conf. on Micro Electro Mechanical Systems* (IEEE) pp 557–80

Yang Y, Nguyen N, Chen N, Lockwood M, Tucker C, Hu H, Bleckmann H, Liu C and Jones D L 2010 Artificial lateral line with biomimetic neuromasts to emulate fish sensing *Bioinspir. Biomim.* **5** 016001